remote sensing

MDPI

Technical Note

Search for Electron Bursts in the Inner Van Allen Belts with the CSES and NOAA POES Satellites

Coralie Neubüser [1,*], Roberto Battiston [2], William Jerome Burger [1], Francesco Maria Follega [2] and Vincenzo Vitale [3]

[1] TIFPA-INFN, Via Sommarive 14, 38123 Trento, Italy
[2] Dipartamento di Fisica, Università degli Studi di Trento, Via Sommarive 14, 38123 Trento, Italy
[3] INFN Sezione di Roma Tor Vergata, 00133 Rome, Italy
* Correspondence: coralie.neubueser@tifpa.infn.it

Abstract: Earthquake monitoring plays a key role in human life protection, especially in highly populated areas of the Earth. First indications have been found in SAMPEX and NOAA satellite data that particle fluxes of trapped electrons in the Van Allen belts can be correlated to seismic activity on the ground. Within the framework of the CSES mission, a systematic analysis of the electron flux, within the invariant phase space in the L-shell and equatorial pitch angle, has started with the goal to identify short-term variations of the flux (particle bursts) in conjunction with seismic activity. This analysis is based on the statistical evaluation of the flux measurements and built to be potentially implemented in an online monitoring system. The first milestone in that direction has been achieved, providing a stable background estimation. With the injection of artificial signals, the efficiency of the method was evaluated and found to be better than 95% for isolated (one per day) and short ($\sim$3 min) signals with a significance $\geq 5\sigma$ above the background. The developed method is set up in a manner to be easily applicable to data from different instruments and satellites. This article presents the studied datasets of the low-energy HEPP instrument onboard the CSES-01 satellite and the electron telescopes of the MEPED detector onboard the NOAA POES-19 satellite, introduces the method for the background estimation, and discusses the first correlation studies of particle bursts with geomagnetic indices obtained within this framework.

Keywords: radiation belt electron precipitation; trapped low-energy particles; statistical analysis of electron flux; correlation of particle bursts with geomagnetic and solar storms

Citation: Neubüser, C.; Battiston, R.; Burger, W.J.; Follega, F.M.; Vitale, V. Search for Electron Bursts in the Inner Van Allen Belts with the CSES and NOAA POES Satellites. *Remote Sens.* **2023**, *15*, 411. https://doi.org/10.3390/rs15020411

Academic Editor: Yunbin Yuan

Received: 12 November 2022
Revised: 16 December 2022
Accepted: 26 December 2022
Published: 9 January 2023

1. Introduction

Short-term electron flux increases (bursts) in the inner Van Allen radiation belt, correlated in time with seismic activity, have been reported by satellites [1–5]. The correlation may be attributed to Doppler-shifted cyclotron resonance interaction between the magnetically trapped electrons and very-low-frequency (VLF) electromagnetic (EM) waves traveling along the magnetic field lines [6]: this phenomenon would describe the observed VLF EM emission and electron flux bursts associated with VLF ground transmitters [7] or atmospheric lightning [8]. The correlation could also be associated with extremely low-frequency (ELF)-VLF EM emissions of seismic origin, as has been reported by the Intercosmic-24 satellite [9]. Still, in order to use these observables in future remote sensing applications, a better understanding of the origin of particle bursts (PBs) detectable in space would require additional modeling and systematic testing using accurate satellite data.

The Detection of Electro-Magnetic Emissions Transmitted from Earthquake Regions (DEMETER) (http://demeter.cnrs-orleans.fr, accessed on 1 November 2022) micro-satellite of the French National Space Agency was the first satellite dedicated to the study of wave–particle interactions associated with natural phenomena and anthropogenic activities [10]. The satellite was launched on 24 June 2004, with a scientific payload including

electromagnetic field sensors and a particle detector, which allow the VLF EM emission and electron flux bursts to be detected at the site of the wave–particle interaction. These observed satellite-correlated wave–particle measurements are associated with VLF transmitters [11,12], atmospheric lightning [13], and seismic phenomena [14]. Electron flux bursts, which could be associated with seismic activity, were correlated in time with broadband VLF emissions. The satellite mission ended on 9 December 2010.

The National Oceanic and Atmospheric Administration (NOAA) Polar Operational Environmental Satellites (POES) (https://www.ngdc.noaa.gov/stp/satellite/poes/, accessed on 1 November 2022) also provide measurements of the electron and proton fluxes in the radiation belts. In addition, the China Seismo-Electromagnetic Satellite (CSES-01) [15] was launched on 2 February 2018, also carrying scientific payloads providing measurements of the electromagnetic fields and radiation belt electrons and protons. We present a study of PBs observed by these different satellites, with the objective of understanding the potential of PBs as a variable that could be associated with the co-seismic or the precursor phenomena associated with earthquakes. Since these satellites produce a large quantity of data that should be treated in real-time in the context of earthquake precursors, data treatment has to be based on well-understood, unbiased procedures. In this paper, the data preparation and the selection of candidate electron PBs are described and illustrated by the results obtained with two different instruments/satellites: the low-energy electron detector of the High-Energy Particle Package (HEPP-L) onboard the CSES-01 satellite and the electron telescopes of the Medium Energy Proton Electron Detector (MEPED) onboard the NOAA POES-19 satellite.

2. Materials and Methods

2.1. Datasets

Wave–particle interactions should result in enhancements of the electron flux within the inner Van Allen belts. The payloads of the two satellites used in this analysis vary in technology, energy resolution, orientation, and acceptance. They have, however, an overlapping energy sensitivity, thus providing complementary information on the electron flux of the inner belts.

2.1.1. HEPP-L on CSES-01

The CSES-01 satellite was launched in 2018 and has been successfully taking data since August 2018. The satellite is Sun-synchronous, orbiting at an altitude of 498–526 km, and circling the Earth about 16 times a day with a 5-day revisiting periodicity. The satellite has multiple payloads that provide measurements of the magnetic field and electromagnetic waves at extremely low (ELF) and very low frequencies (VLF) [15–17]. The particle detectors instead are focused on the detection of protons, electrons, and heavy nuclei and are the HEPD, HEPP-H, and HEPP-L instruments. All payloads onboard the satellite are switched off at latitudes below -65° and above 65°. The HEPP-L detector consists of 9 silicon slice units that contain a thin and a thick silicon sensor of 300 µm and 2 mm in thickness, respectively, each. The difference in the deposited energy $\frac{dE}{dx}$ within the two sensors is used in order to distinguish particle species, which results in an efficiency of 96.7% for electrons [18]. The silicon units can be divided into two types, featuring narrow (5 units) and wide (4 units) collimators that define the field of view. The "narrow channels" have each an opening angle of 13° and the "wide channels" of 30°. The two types are placed along two arcs, each of the telescopes pointing in a slightly different direction. Both arcs are oriented on the satellite at 70° from zenith and perpendicular to the velocity vector. The local pitch angle distributions for the first (0) and last (8) channel are shown in Figure 1a and confirm the complementarity of their measurements.

The electron flux data available are so-called Level 3 calibrated data; the electron rates are converted into fluxes (available from https://leos.ac.cn, accessed on 29 March 2022). The electron fluxes are measured every second by each silicon unit separately and are divided into 256 energy bins, each covering a range of 11 keV. The telemetry provides

the satellite position (longitude, latitude, altitude, and L-shell). The "narrow" and "wide" channels have a different acceptance, even though the local pitch angle range widely overlaps. In this study, we analyzed each channel independently.

2.1.2. NOAA POES-19 MEPED

The NOAA POES satellites are Sun-synchronous and orbit the Earth about 13 times a day at an altitude of 847–874 km. All POES satellites contain two main instruments that measure particle fluxes, the Total Energy Detector (TED) and the Medium Energy Proton and Electron Detector (MEPED). The MEPED is specifically designed to measure electrons and protons within the radiation belts and contains two proton and electron telescopes. The electron telescopes consist of fully depleted silicon surface barrier detectors with an area of 25 mm^2 and a thickness of 700 µm [19], which allows full absorption of electrons with energies up to 2.5 MeV, and they are oriented towards zenith (0°) and perpendicular to zenith (90°). The MEPED has an additional inclination angle of 9° and 9.08°. The resulting pitch angle ranges are shown in Figure 1b. A nickel foil across the entrance window is used in order to prevent low-energy < 100 keV protons from entering, while protons in the energy range of 200 to 2700 keV are counted as electrons and make up to 20% of the measured flux [20]. The telescopes have collimators that define an opening angle of 30°.

The data of the instruments onboard the NOAA POES-19 satellite are available from 2010 until the present (https://www.ngdc.noaa.gov/stp/satellite/poes/dataaccess.html, accessed on 27 November 2021) and contain electron fluxes measured above 4 different energy thresholds every 2 s. In addition, information on the satellite position in longitude, latitude, and altitude, the magnetic field strength, and L-shells is provided.

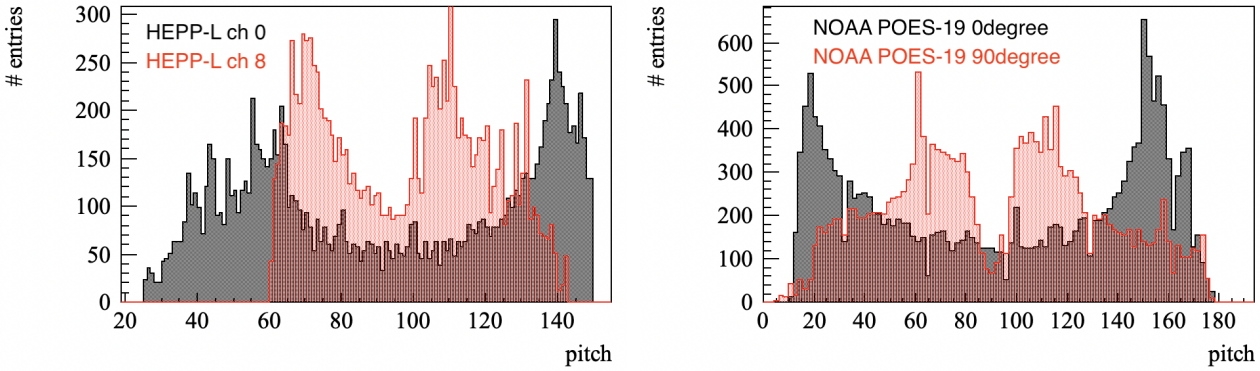

(**a**) CSES HEPP-L (**b**) NOAA POES-19

Figure 1. Local pitch angle distributions (**a**) for Channels 0 and 8 of HEPP-L and (**b**) for the 0° and 90° telescopes of the MEPED, for one day in August 2020.

2.2. Data Preparation

For this analysis, we selected data from the period 2019 to 2022. In order to compare the various datasets, a special data processing was implemented. The HEPP-L fluxes are given per energy bin per second, while the NOAA POES-19 telescope fluxes were measured above energy thresholds. Since the HEPP-L data provide more than enough information, we applied artificial offline energy thresholds by summing up the flux values per second above three chosen threshold values. These values are given in Table 1, together with the geometric factors used to convert electron counts N_{counts} to electron fluxes ϕ, following the relation:

$$\phi = \frac{N_{counts}}{f_{geom}}. \quad (1)$$

Table 1. Summary of detector specifications.

Instrument	Telescope	f_{geom} (cm²·s·sr)	Measurement Rate (Hz)	E_{thr} (MeV)
MEPED	0° 90°	$\frac{(1.24/1.44/0.75/0.55)^1}{100}$ [19]	1/2	0.04/0.13/0.29/0.61
HEPP-L	narrow channels: 0, 2, 4, 6, 8 wide channels: 1, 3, 5, 7	0.12 0.73 [21]	1	0.1/0.28/0.46

[1] From low- to high-energy threshold.

2.2.1. Study of Fluxes in the Invariant Phase Space

In order to study the electron flux as a function of time and identify sudden variations, the flux is studied on a daily basis within an adiabatic invariant phase space, using the variables: L-shell and equatorial pitch angle α_{eq} , following the examples of [3,4] with the adjustment of using the equatorial instead of the local pitch angles, which renders the background estimates fully invariant. The L-shell describes the set of magnetic field lines that cross the Earth's magnetic equator at a number of Earth radii equal to the L-shell value. Satellites with polar orbits pass over a large range of geomagnetic latitudes, thus magnetic field lines and L-shells. The values used here are based on the IGRF model [22,23] and were provided in the data stream for both NOAA and CSES data. While the local pitch angle (α_{loc}) refers to the angle between the particle trajectory and the local direction of the magnetic field line, α_{eq} is the angle between the particle trajectory and the projected magnetic field line at the Equator. This variable can be calculated in the dipole approximation of the Earth's magnetic field, using the relation:

$$\frac{sin^2(\alpha_{loc})}{B} = \frac{sin^2(\alpha_{eq})}{B_{eq}} \tag{2}$$

with the magnetic field at the Equator $B_{eq} = M/L^3$ [24] and the dipole magnetic moment $M = 0.311653\,\mathrm{G}$. From these relations, we can derive the solution for α_{eq} as:

$$\alpha_{eq} = \begin{cases} asin\left(sin(\alpha_{loc})\sqrt{\frac{B_{eq}}{B}}\right), & \alpha_{loc} \leq \frac{\pi}{2} \\ \pi - asin\left(sin(\alpha_{loc})\sqrt{\frac{B_{eq}}{B}}\right), & \alpha > \frac{\pi}{2} \end{cases}. \tag{3}$$

The local magnetic field B is provided in the NOAA data stream and was calculated for the CSES data using the IGRF model Version 13 [23] with a fixed altitude of 507 km. The chosen resolution in the L-α_{eq} phase space is displayed in Figure 2, which shows the flux populations for the different instruments over one day excluding the region of the South Atlantic Anomaly (SAA), cutting on the local magnetic field. The cut was adapted for the two instruments to exclude a similar geographic region. Overall, the resolution in α_{eq} was chosen to reflect the detectors' accuracy, while the binning in the L-shell was set to 1 Earth radius (R_E) for $L > 2$ and to 0.2 Earth radii steps for $1 < L < 2$. This choice was based on the fact that we are mostly interested in flux measurements for $L < 2$, as we will discuss in Section 2.3.

2.2.2. Time Integration

We integrated the fluxes in time. The measurement rates for the MEPED and HEPP-L detectors are 0.5 and 1 Hz, respectively. Due to the low electron rates, the measured fluxes per second often correspond to zero particle counts in the detector. This results in largely fluctuating flux values and complicates the search for outliers. Therefore, we integrated the fluxes in 16 s, within the α_{eq} bins, and assigned the average L-shell position to the integrated flux value. The effect of this integration is shown in Figure 3 for all datasets,

for a given L-α_{eq} cell. The grey distributions corresponds to the flux values per second for the HEPP-L data and per 2 s for the NOAA POES-19 data. The yellow distributions show the distributions after the 16 s time integration. The binning of the histograms corresponds to the number of electron counts, using the geometrical factors given in Table 1. Two effects were observed: First, the total number of entries is reduced due to the integration in time. Second, the distributions change their maximum from zero to higher values, which is closer to a Gaussian distribution. Another effect of the time integration is the clearer separation of exceptionally high flux values from the bulk of the distribution. This is clearly visible in Figure 3c.

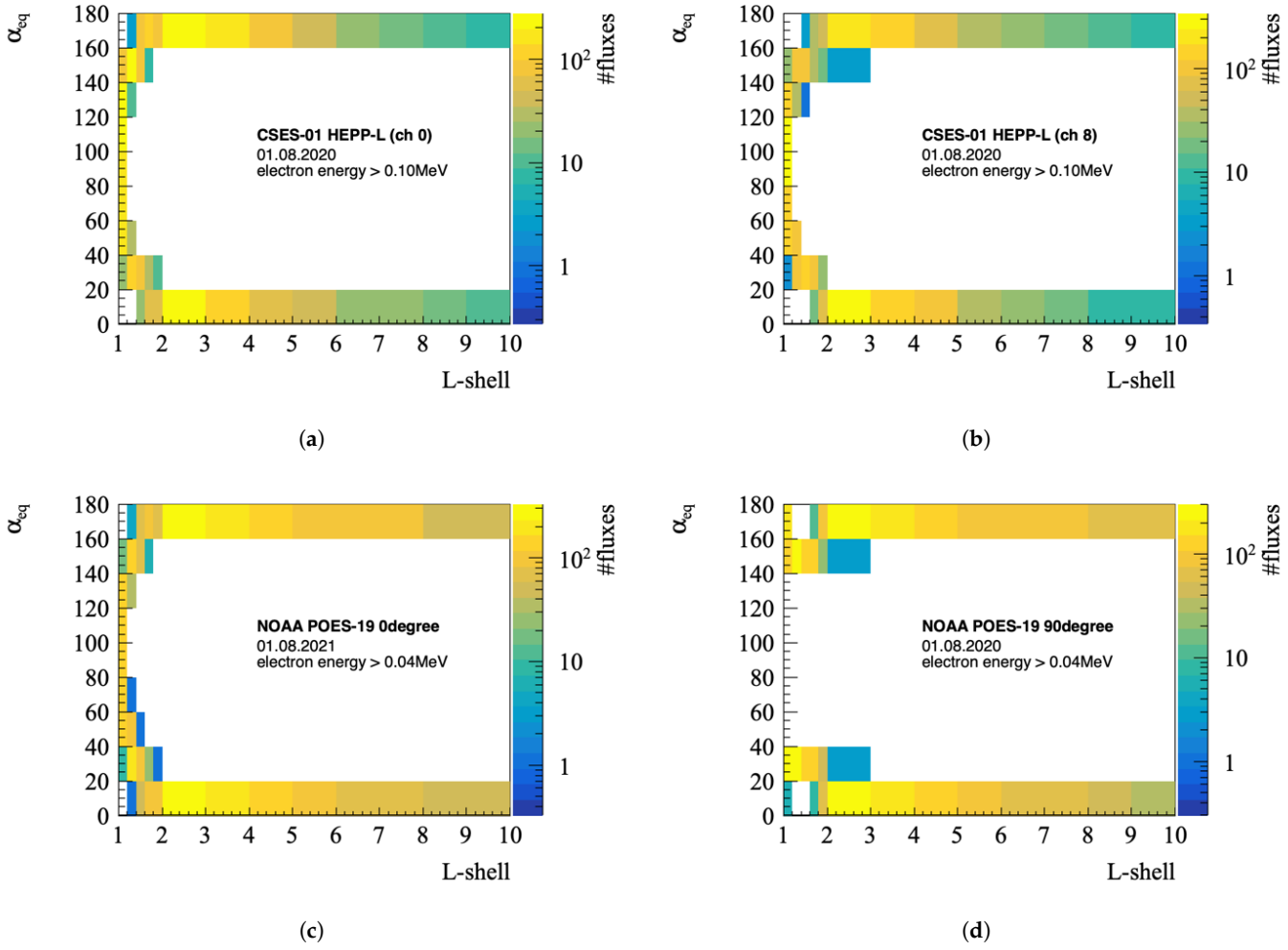

Figure 2. The accumulated flux measurements in one day in the L-α_{eq} phase space for (**a**) CSES HEPP-L, Channel 0, (**b**) CSES HEPP-L, Channel 8, (**c**) NOAA POES-19 0°, and (**d**) NOAA POES-19 90°: data from the SAA are rejected cutting on the local magnetic field at 22 and 25 knT for the NOAA and CSES data, respectively. The color scale shows the number of electron flux measurements in each cell during a day.

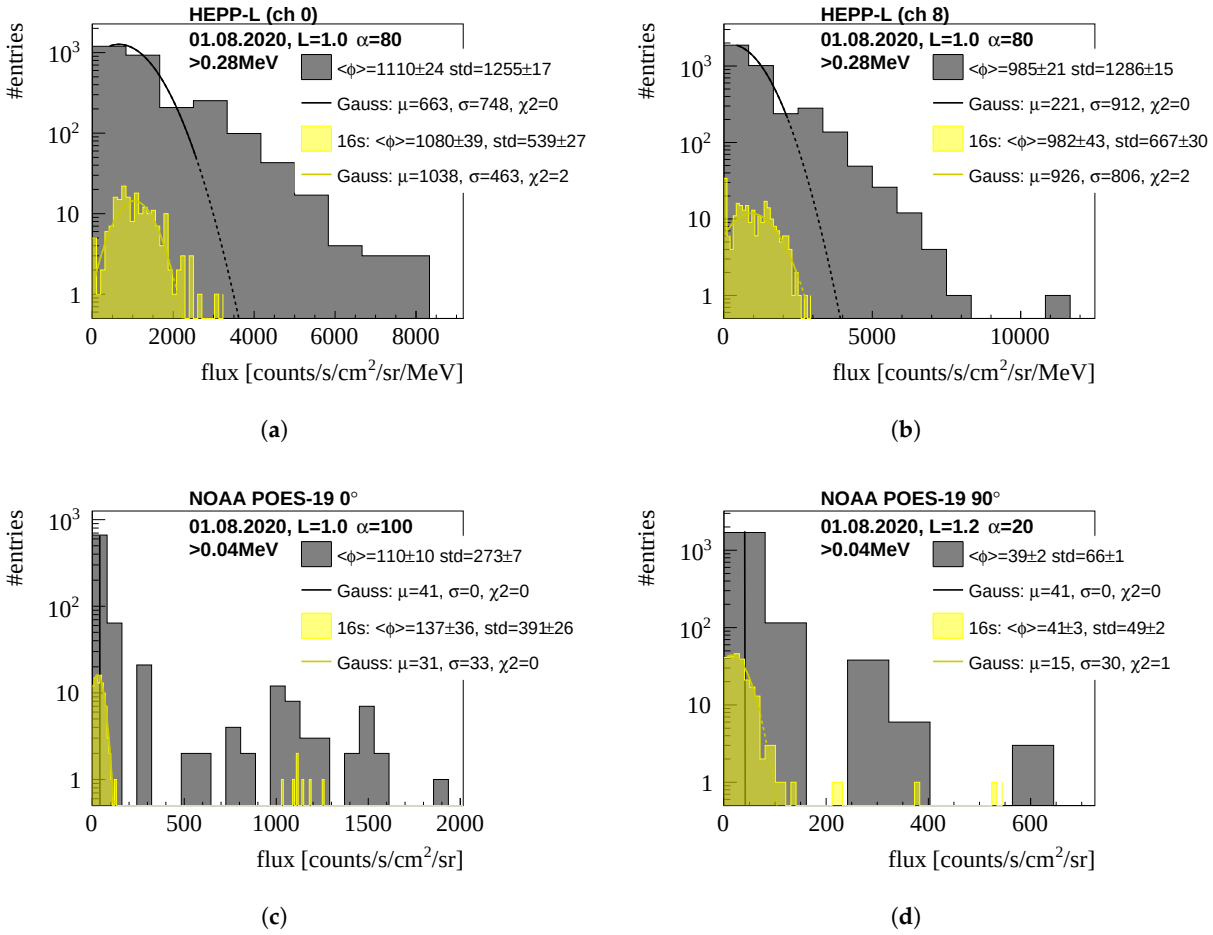

Figure 3. Flux distributions above different energy thresholds in specific L-α cells (see legends) measured with (**a**) CSES HEPP-L, Channel 0, (**b**) CSES HEPP-L, Channel 8, (**c**) NOAA POES-19 0°, and (**d**) NOAA-POES 19 90° instruments on 1 August 2020. The grey and yellow distributions correspond to time integration windows of 1(2) s and 16 s, respectively. The curves correspond to Gaussian fits.

2.3. Daily Background Estimates

In order to identify particle bursts within a series of flux measurements, we used daily background estimates in the adiabatic invariant phase space, defined by the L-shell and equatorial pitch angle α_{eq} . The phase space during one day is shown in Figure 2 for both instruments. The color code represents the number of fluxes within each cell. Overall, the NOAA POES-19 0° detector shows a similar coverage as the CSES HEPP-L detectors. The main difference lies in the available statistics at high L-shell values, which is lower for CSES due to the lower altitude of the satellite orbit and the limit to absolute latitudes $< 75°$, while the NOAA POES-19 satellite provides observations up to 80°.

The geographical location of the L-α_{eq} cells is visualized in Figure 4 for two channels of the HEPP-L detector in (a) and (b). The color code shows the L-α_{eq} cell index, which corresponds to different regions in the L-α_{eq} space. The translation of the index in the L-α_{eq} space is shown in Figure 4c. The mirroring of the color code, between Figure 4a,b, with respect to the geomagnetic equator, reflects the symmetry in the pointing direction of the different channels of the HEPP-L instrument. The fluxes with the same L-α_{eq} cell index were collected over one day, and the distributions were analyzed.

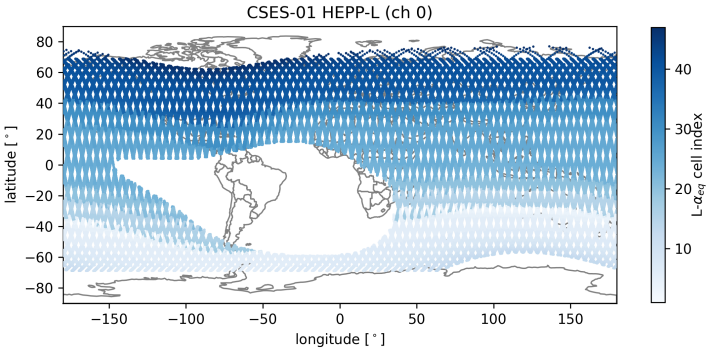

(**a**)

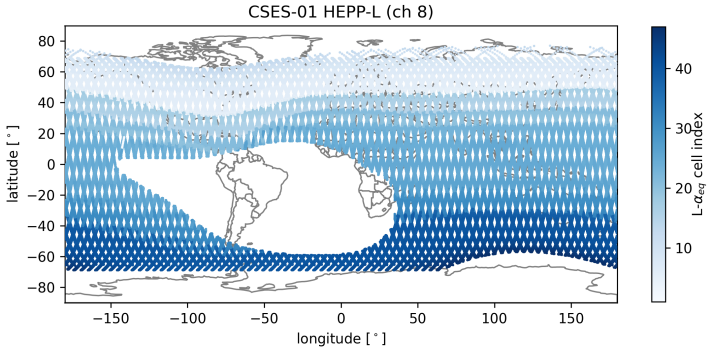

(**b**)

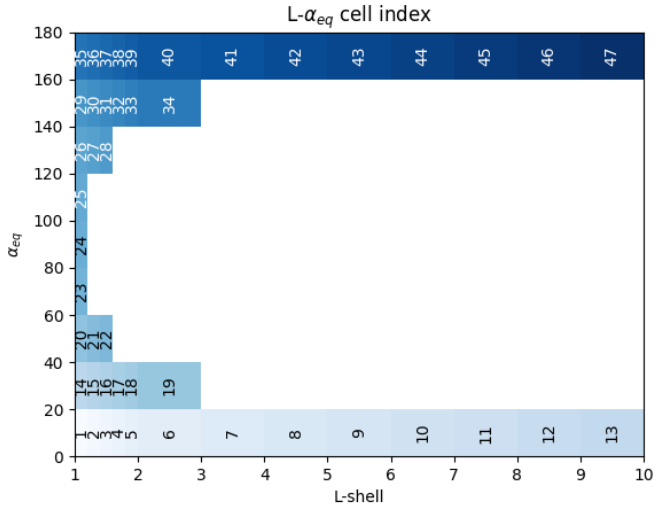

(**c**)

Figure 4. Geographical location of the L-α cells for Channel 0 (**a**) and Channel 8 (**b**) of CSES HEPP-L after the SAA rejection during the year 2019. The color scale represents the L-α_{eq} cell index, thus reflecting the invariant phase space, which are compared to each other. (**c**) The cell index in the L-α_{eq} phase space.

We tested different methods to describe the bulk of the flux distributions and define an effective threshold above which only outliers can be found. Due to the varying shapes of the distributions, multiple methods were tested and evaluated in terms of stability and efficiency. The main tested methods were: (1) a simple mean and standard deviation (std) with a resulting threshold d_{mean} as the sum of the mean plus three-times the std, (2) a Gaussian fit with a threshold d_{gauss} defined as the sum of the most-probable value of

the fit μ plus three-times the standard deviation σ, and (3) the mean and std of a restricted flux range, defined as the flux value below which the lowest 50 % of all flux values of the histogram are contained (rms50) multiplied by three. This multiplication factor was chosen in order to effectively exclude all events found in the tails of the distribution while being high enough to reject the flux values within the bulk of the distribution. The impact of this factor will be further discussed in Section 3.1. The corresponding threshold d_{rms50} was then calculated as the sum of the mean plus three-times the std in the flux range from 0 to $3 \times$ rms50.

For each flux distribution in every L-α_{eq} cell, a minimum statistic of 50 entries was required for this analysis to ensure a good stability of the thresholds and a maximum coverage of the L-α_{eq} range. This requirement slightly reduced the L-shell range of the CSES HEPP-L data.

In Figure 5, we show the example of two flux distributions with (b) and without (a) a significant tail together with the thresholds (vertical lines) corresponding to the algorithms described above. The Gaussian fit and the resulting threshold caught the tails very effectively. However, in about 10% of the cases, this algorithm failed. The threshold set using the simple mean and std (straight line) was highly impacted by large tails in the distributions and resulted in losing potentially interesting events. The threshold estimated with the mean and std in a limited flux range (dashed–dotted line) did not suffer from this effect and showed similar values as the Gaussian fit.

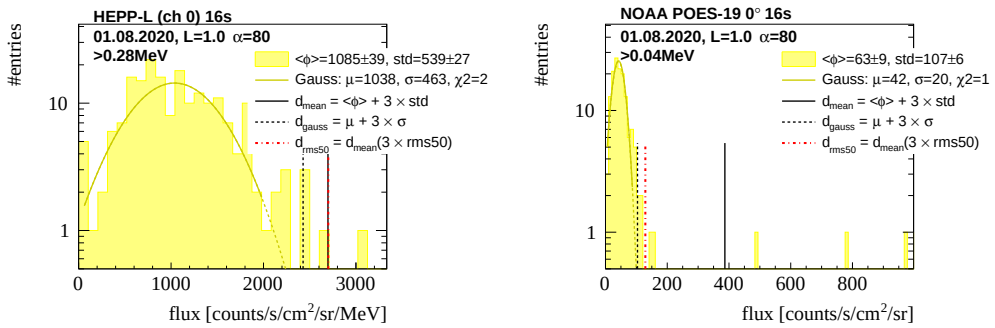

(**a**) CSES HEPP-L, channel 0 (**b**) NOAA POES-19 0°

Figure 5. Flux distributions measured with (**a**) CSES HEPP-L, Channel 0, and (**b**) NOAA POES-19 0° above a chosen energy threshold (given in the legend) and specific L-α_{eq} cell: $1.0 \leq L < 1.2$ and $80° \leq \alpha_{eq} < 100°$. The curves correspond to a Gaussian fit, and the straight, dotted, and dotted–dashed lines mark d_{mean}, d_{gauss}, and d_{rms50}, respectively.

2.4. Clustering

This algorithm was used to cluster significant measurements, which were identified to be close in time. This tool can form clusters within, as well as across L-α_{eq} bins and energies. In this way, we can form clusters using measurements coming from different L-α_{eq} bins or exploit the properties of the adiabatic invariants. We chose to cluster across L-α_{eq} bins, but for each energy threshold separately.

The working principle of the algorithm is simple, and it uses the DBSCAN method [25–27], which is commonly used to perform fast and accurate clustering [28,29]. The algorithm is described schematically in Figure 6 and is summarized in the following steps:

- The time sequence is scanned to find events above the threshold (one of the four defined before). These events are called "seeds".
- If two subsequent flux measurements are seeds, then a time window is opened. The window starts at the time of the second seed and extends for the next M seconds.
- If another pair of subsequent seeds is found in the time window, another window is opened, and the seed search continues. This procedure is iterated until no more pairs of subsequent seeds are found within M seconds from the previous.

- After the stop of the iterative procedure, the measurements within half a window from the first and last seed are added to the cluster.

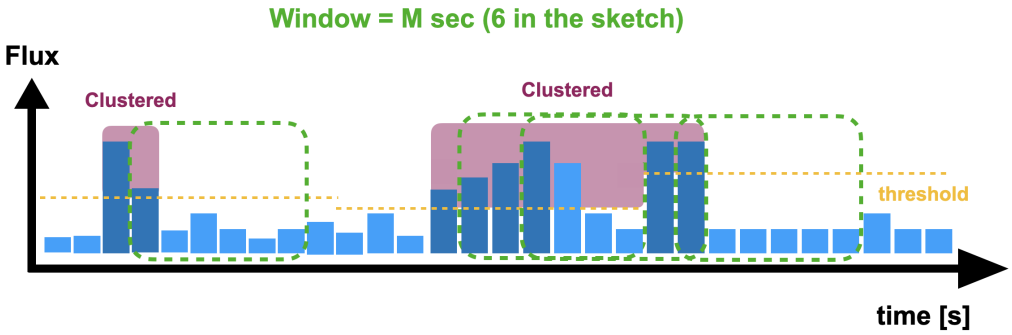

Figure 6. A sketch of the working principle of the clustering algorithm. The time sequence of fluxes is scanned, and seeds (dark blue) are identified as fluxes above the threshold (orange), set per L-α_{eq} bin. The threshold changes in time due to the crossing from one to another L-α_{eq} bin. In this sketch, the window size is $M = 6$ s, counted from the second of the subsequent seeds.

The window size was tested between 50 and 1000 s and was finally chosen to be 100 s. This allowed an efficient collection of large close-by signals while ensuring temporal discrimination and was tested via visual inspection of the flux–time profiles. These clusters can also be called *particle* or *electron bursts*, and both terms are used equivalently in the following.

2.5. Testing of Sensitivity and Efficiency

In order to evaluate the sensitivity and efficiency of this method, artificial signals were introduced into the data and their discovery rate used as an indicator for the efficiency of the algorithm. These artificial signals were chosen to be 160 s long (ten subsequent flux measurements), followed a step function, and were introduced across all energy thresholds. The signal height was chosen in terms of significance with respect to the specific L-α_{eq} cell traversed by the satellite at a given moment. Hereby, it was made sure that these signals were introduced in regions that allowed for a background estimation; see Section 2.3. The procedure is divided into the following steps:

1. The time of the artificial signal is randomly chosen within the available time period (i.e., outside the SAA and within an L-shell range from 1 to 5).
2. Within that time period, the artificial signal replaces the original measurement with a value based on the average and standard deviation from the background estimation in that L-α_{eq} cell.
3. The background estimation is repeated on the new dataset, which includes the artificial signals.
4. The flux selection based on the new background estimation (with a threshold of d_{rms50}) is applied, and the number of artificial signals that are identified is counted and compared to the total number of introduced artificial signals.

Examples of the flux–time profiles with added artificial signals are shown in Figure 7. While the original data are shown as dots, the artificial signals are represented as triangles. The open triangles mark the signals that were correctly identified with our method. The comparison between Figure 7a,b shows that signals with a lower significance in Figure 7a are visually harder to identify within the distribution and are less often correctly identified with respect to the higher significant signals, shown in Figure 7b. Due to the change of the L-α_{eq} cell during the 160 s-long signals, a shift in the flux values can be observed.

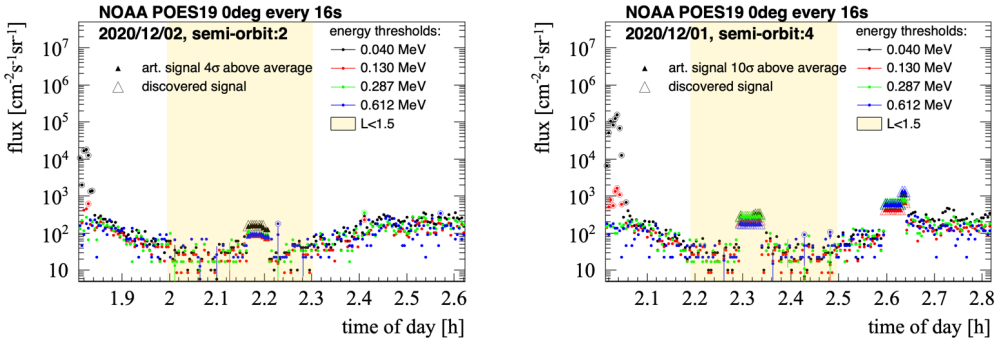

(**a**) (**b**)

Figure 7. Flux–time profiles of NOAA POES-19 0° with all measured fluxes (dots) above four energy thresholds, given in different colors. The open circles mark the fluxes that were selected above the background. (**a**) Profile from 2 December 2020 with an added artificial signal (filled triangles) with a significance of 4σ. (**b**) Profile from 1 December 2020 with two added artificial signals with a significance of 10σ. The open triangles mark the artificial fluxes that were correctly identified, and the yellow area shows the low (<1.5) L-shell region.

3. Results

The efficiency of the described electron burst search is mitigated by two main effects: the coverage of the L-α_{eq} phase space and the accuracy of the description of the background and, consequently, of the stability of the thresholds defined. Both effects were quantified, and the results are summarized in Section 3.1.

Additionally, a study of the correlation between the electron bursts that were found and the geomagnetic indices was performed in order to verify the sensitivity to magnetospheric instabilities due to geomagnetic storms and solar winds. The results are summarized in Section 3.2.

3.1. Efficiency and Sensitivity

A stable background estimation in L-α_{eq} cells requires the minimum statistics of the flux measurements in that part of the phase space. The impact of the chosen lower limit of 50 flux measurements per L-α_{eq} cell is summarized for all datasets in Table 2. Overall, 60 to 77 % of the L-α_{eq} space was probed for the electron burst search, while only 5 to 8 % of the flux measurements were lost due to a lack of the statistic in the remaining 23 to 40 % L-α_{eq} cells. These values were extracted from three months of data, one month per year, and were found to be very stable in time.

Table 2. Flux losses and L-α_{eq} coverage of background estimation with a minimum of 50 events per L-α_{eq} cell for all datasets, estimated over three months (one month per year) of data.

Dataset	L-α_{eq} Coverage (%)	Flux Losses (%)
NOAA POES-19 0°	76.5	4.8
NOAA POES-19 90°	64.5	5.9
HEPP-L channel 0	60.8	6.6
HEPP-L channel 8	59.9	7.8

The efficiency of finding signals of a certain significance above the background was tested as described in Section 2.5. The signal significance was based on the chosen methods: simple mean/std or mean/std in the restricted flux range (3 × rms50), and the threshold was set to 3σ for the selection. The comparison between the two methods is shown in Figure 8a in terms of the detection rate for the introduced signals, during a time period of 2 months, introducing one artificial signal per day. Using signal significances ranging

from 4 to 8σ and using 3 $\times$ rms50, the background estimation within a restricted flux range exhibited a reduced variance in the recovery rate when compared to the simple mean/std method. In addition, a recovery rate of 95% was obtained using the restricted mean/std method. On the basis of these results, the method of the restricted mean/std was chosen as the baseline for ongoing electron burst searches.

Figure 8b shows the comparison of the efficiency as a function of the number of artificial signals introduced during one day. The number of tested days was hereby higher (double) for single signals added per day in order to increase the statistics and reach stable results. All efficiencies were tested against larger statistics and found to be unaffected.

It is expected that the background estimation degrades with an increasing number of bursts introduced during a day, due to the increased mean and std values in the background estimations. This effect results in a lowered sensitivity, especially for signals with low significance. The efficiency for the recovery of 5σ signals dropped from 95 to 70 % when introducing 10 signals instead of 1 signal per day. Although these tests showed no dependence of the efficiency on the energy threshold, the efficiency was found to be lower in lower L-shells ($L < 2$), as can be seen in Figure 8c. This can be explained by the larger number of electron bursts observed in that region, which already negatively affected the background estimation and led to a reduced sensitivity to smaller signals. The L-shell distribution of all electron bursts that were found with the NOAA POES-19 0° data is shown in Figure 8d: it features a peak of electron bursts at $1.1 < L < 1.6$.

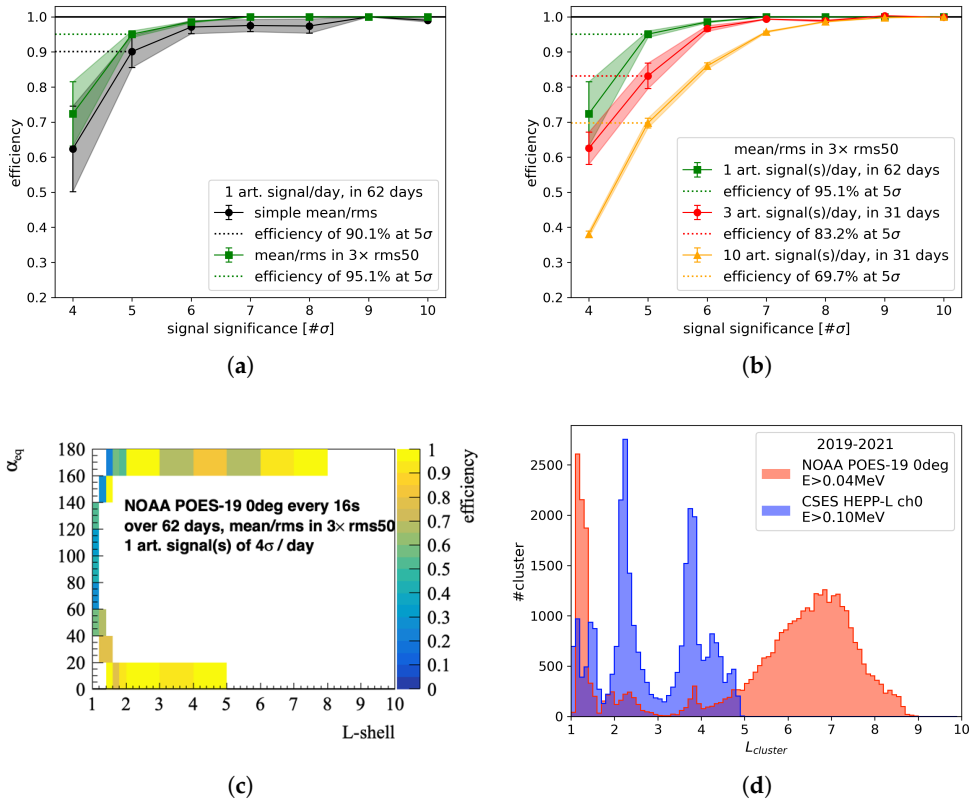

Figure 8. Identification the efficiency of artificial signals introduced to NOAA POES-19 0° data. (**a**) Comparison of the efficiency for the simple mean/std method (black) and the mean/std taken from a restricted flux range (green). (**b**) Reduction in sensitivity for 1, 3, and 10 artificial signals introduced per day. The error bands correspond to the variance observed over the full tested time period. (**c**) Efficiency map in L-α_{eq} for 1 artificial signal of 4 σ significance. (**d**) L-shell distribution of the found electron bursts (cluster) over 3 years of NOAA POES-19 0° (blue) and CSES HEPP-L Channel 0 (red) data.

3.2. Correlation of Particle Bursts and Geomagnetic Indices

We attempted to determine the correlation between the electron bursts that were found and the presence of geomagnetic storms or solar winds. In this analysis, we focused on the outer radiation belts ($L > 3$), which are expected to be more strongly impacted due to their physically higher exposure [30]. As indicators for solar storms, we chose the k_P index (https://www.gfz-potsdam.de/en/kp-index/, accessed on 11 January 2022) [31], which is based on 13 magnetic observatories and is a reliable proxy for the energy input from the solar wind to Earth. The *SME* index (http://supermag.jhuapl.edu/, accessed on 3 March 2022) (previously AE) is based on ∼100 ground stations and is a proxy for geomagnetic storms by sampling the thermal portion of the magnetotail plasma sheet [32]. The D_{st} index (https://wdc.kugi.kyoto-u.ac.jp/dstdir/, accessed on 7 March 2022) is a measure of variation in the geomagnetic field due to the equatorial ring current and has a value lower than −50 in the case of storm-level disturbances. These indices are based on the global network of the SuperMAG [33] and of INTERMAGNET [34] magnetometers.

Figures 10 and 10 show the correlations between the daily number of electron bursts with the geomagnetic indices for the NOAA POES-19 0° data and the CSES HEPP-L Channel 0 data, respectively. The total number of electron bursts per day were compared to the daily averages of the *SME* and D_{st} indices and the maximum k_P index of the day. The electron bursts in the NOAA data showed a clear correlation with the indices in the outer Van Allen belt at $L \geq 3$ (right column in Figure 10), while the dependence was less pronounced in the HEPP-L data. This can be explained by the better coverage of high L-shell regions with the NOAA POES-19 satellite. The distribution of the L-shell of reconstructed particle bursts is shown in Figure 8d. While the L-shell distribution of the electron bursts in the NOAA data showed two main peaks at 1.2–1.6 and 5–8, the electron bursts of the HEPP-L data were more often found at 2–3 or around 4. The difference in the peak heights at different L-shells for the electron bursts from the NOAA POES-19 and HEPP-L Channel 0 data can be explained by the difference in their orientation on the satellites. The electron telescope of NOAA POES-19 points towards zenith, thus is sensitive to low L-shells at the local mirror points of trapped electrons. The HEPP-L detector is oriented 70° with respect to zenith, which shifts the sensitivity to the high-electron-flux regions along the field lines to higher L-shells. The HEPP-L detector does not find bursts at $L > 5$, since, due to the lower altitude of the satellite, higher L-shells are crossed for shorter periods of time. This results in too low statistics for the background estimation and prevents the reconstruction of electron bursts.

The correlation of electron bursts with geomagnetic indices was also tested in the inner Van Allen belt ($L < 3$); see the left column of Figures 10 and 10. Here, no clear correlation with the tested geomagnetic indices could be found, neither for NOAA POES-19 nor HEPP-L data.

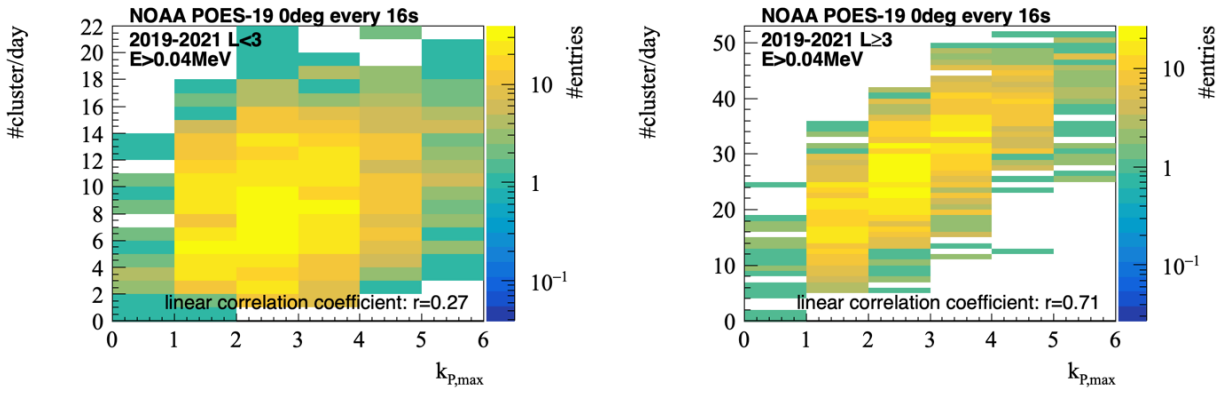

(**a**) (**b**)

Figure 9. *Cont.*

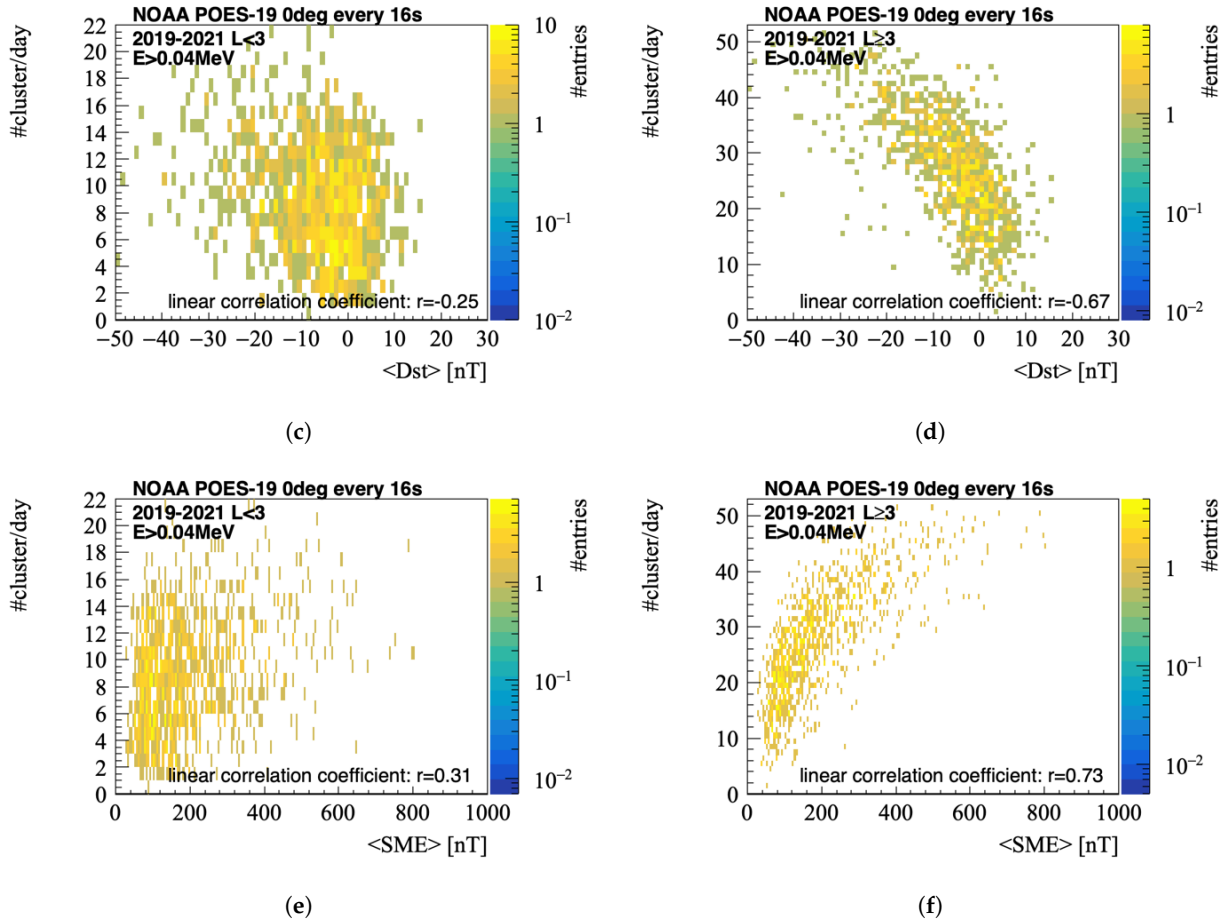

Figure 9. Correlation between geomagnetic indices: k_P (**a**,**b**), D_{st} (**c**,**d**), and SME (**e**,**f**) and the number of electron bursts per day (**a**,**c**,**e**) at $L < 3$ and (**b**,**d**,**f**) at $L \geq 3$ for NOAA POES-19 0°. The linear correlation coefficients are recorded in the plots.

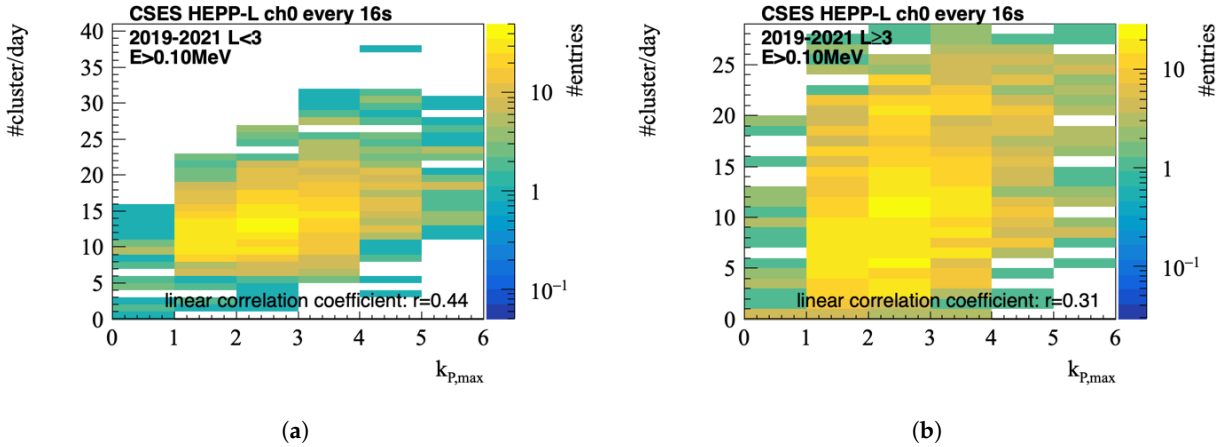

Figure 10. *Cont.*

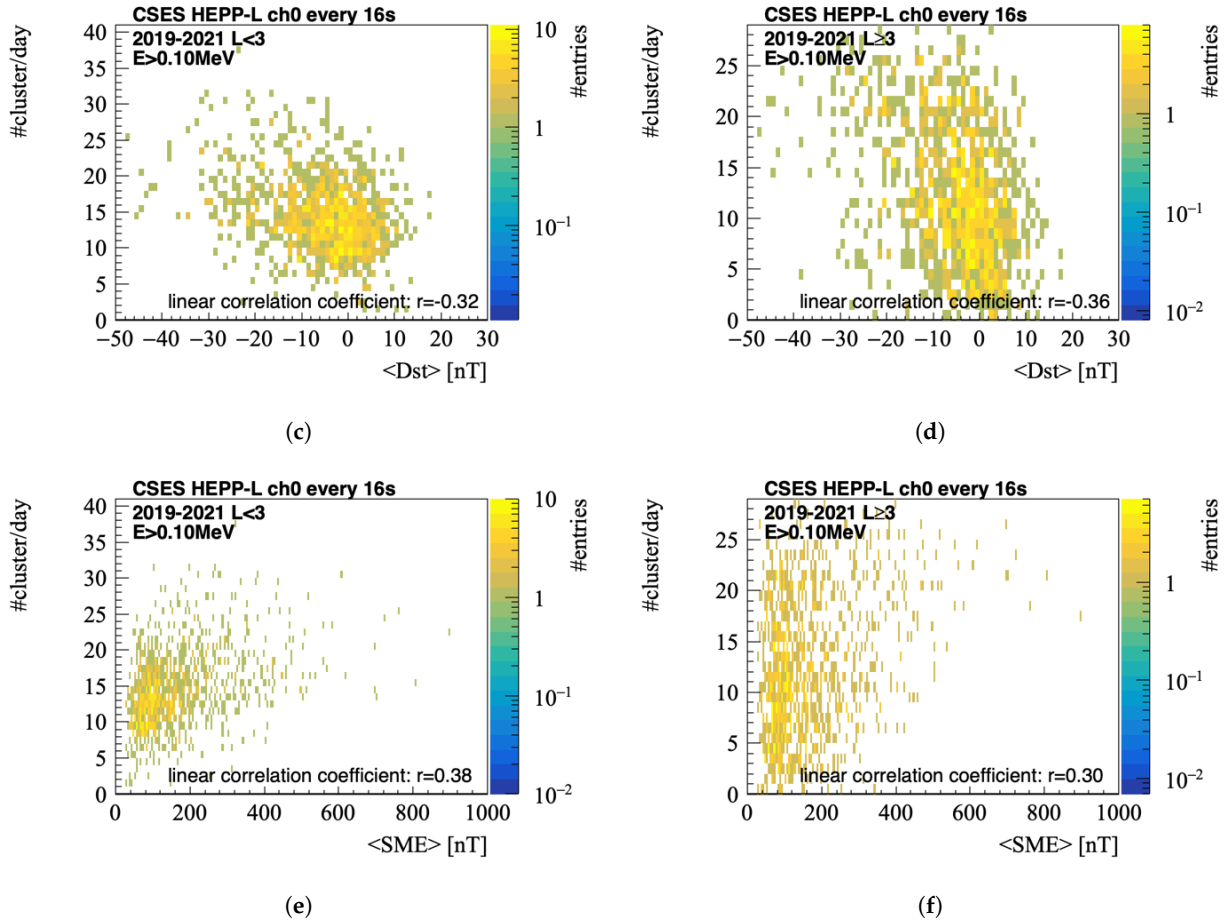

Figure 10. Correlation between geomagnetic indices: k_P (**a**,**b**), D_{st} (**c**,**d**), and SME (**e**,**f**) and the number of electron bursts per day (**a**,**c**,**e**) at $L < 3$ and (**b**,**d**,**f**) at $L \geq 3$ for Channel 0 of HEPP-L. The linear correlation coefficients can be read within the plots.

4. Discussion

A method was developed to identify short-term electron flux increases using datasets from different satellites and detector types. The efficiency of this method depends on the coverage and stability of the background estimation in the L-α_{eq} phase space. We estimated the flux losses due to the accessible L-α_{eq} cells between 5 and 8%, and we detected an efficiency increase for signals at higher L-shells. Overall, an efficiency of 95% could be achieved for signals 5σ above the background and efficiencies above 95% for signals above 7σ, independent of the total number of artificial signals introduced per day.

A study of the correlation between the number of electron bursts per day and the geomagnetic indices confirmed the sensitivity of the particle bursts to the activity in the magnetosphere, although this sensitivity appears to be confined within high L-shells, with $L > 3$.

The large quantity of data provided by the CSES mission allows for a statistical analysis of particle burst properties, which is of essence for real-time monitoring of seismic events. The method described represents the first step in that direction. The correct assignment of PBs to EQs requires additional measurements, combining the detection of VLF/ELF EM emissions, plasma waves, and changes in the frequency line resonance frequency, which is the focus of future analysis activities.

Author Contributions: Conceptualization, C.N.; methodology and software, C.N., F.M.F. and V.V.; validation, C.N. and V.V.; data curation, C.N.; writing—original draft preparation, C.N., F.M.F. and W.J.B.; writing—review and editing, C.N., W.J.B., R.B. and V.V.; project administration and supervision, R.B. All authors have read and agreed to the published version of the manuscript.

Funding: This work was supported by the Italian Space Agency in the framework of the "Accordo Attuativo 2020-32.HH.0 Limadou Scienzaþ" (CUP F19C20000110005) and the ASI-INFN Agreement No. 2014-037-R.0, addendum 2014-037-R-1-2017. This research was partially funded through the CAESAR project by the Italian Space Agency and the National Institute of Astrophysics through the ASI-INAF No. 2020-35-HH.0 agreement for the development of the ASPIS prototype of the Scientific Data Center for Space Weather.

Data Availability Statement: The data presented in this study are available upon request from the corresponding author. The data are not publicly available due to the need for storage resources provided by the INFN CNAF facility, which requires an account for access.

Acknowledgments: The authors wish to thank A. Parmentier, M. Piersanti, and Z. Zhang for their valuable input and collaboration. This work made use of data from the CSES mission, a project funded by the China National Space Administration (CNSA), the China Earthquake Administration (CEA), in collaboration with the Italian Space Agency (ASI), the National Institute for Nuclear Physics (INFN), the Institute for Applied Physics (IFAC-CNR), and the Institute for Space Astrophysics and Planetology (INAF-IAPS). POES data were provided by the NOAA National Geophysical Data Center.

Conflicts of Interest: The authors declare no conflict of interest.

References

1. Aleksandrin, S.Y.; Galper, A.M.; Grishantzeva, L.A.; Koldashov, S.V.; Maslennikov, L.V.; Murashov, A.M.; Picozza, P.; Sgrigna, V.; Voronov, S.A. High-energy charged paricle burst in near-Earth space as earthquake precursors. *Ann. Geophys.* **2003**, *21*, 597–602. [CrossRef]
2. Pulinets, S.A.; Boyarchuk, K. *Ionospheric Precursors of Earthquakes*; Springer: Berlin/Heidelberg, Germany, 2004.
3. Sgrigna, V.; Carota, L.; Conti, L.; Corsi, M.; Galper, A.; Koldashov, S.; Murashov, A.; Picozza, P.; Scrimaglio, R.; Stagni, L. Correlations between earthquakes and anomalous particle bursts from SAMPEX/PET satellite observations. *J. Atmos. Sol. Terr. Phys.* **2005**, *67*, 1448–1462. [CrossRef]
4. Battiston, R.; Vitale, V. First evidence for correlations between electron fluxes measured by NOAA-POES satellites and large seismic events. *Nucl. Phys. Proc. Suppl.* **2013**, *243–244*, 249–257. [CrossRef]
5. Chakraborty, S.; Sasmal, S.; Basak, T.; Chakrabarti, S.K. Comparative study of charged particle precipitation from Van Allen radiation belts as observed by NOAA satellites during a land earthquake and an ocean earthquake. *Adv. Space Res.* **2019**, *64*, 719–732. [CrossRef]
6. Brice, N. Fundamentals of very low frequency emission generation mechanisms. *J. Geophys. Res.* **1964**, *69*, 4515–4522. [CrossRef]
7. Molchanov, O.A.; Mazhaeva, O.A.; Goliavin, A.N.; Hayakawa, M. Observation by the Intercosmos-24 satellite of ELF-VLF electromagnetic emissions associated with earthquakes. *Ann. Geophys.* **1993**, *11*, 431–440.
8. Imhof, W.L.; Reagan, J.B.; Voss, H.D.; Gaines, E.E.; Datlowe, D.W.; Mobilia, J.; Helliwell, R.A.; Inan, U.S.; Katsufrakis, J.; Joiner, R.G. Direct observation of radiation belt electrons precipitated by the controlled injection of VLF signals from a ground-based transmitter. *Geophys. Res. Lett.* **1983**, *10*, 361–364. [CrossRef]
9. Voss, H.D.; Imhof, W.L.; Walt, M.; Mobilia, J.; Gaines, E.E.; Reagan, J.B.; Inan, U.S.; Helliwell, R.A.; Carpenter, D.L.; Katsufrakis, J.P.; et al. Lightning-induced electron precipitation. *Nature* **1984**, *312*, 740–742. [CrossRef]
10. Parrot, M. Special issue of Planetary and Space Science 'DEMETER'. *Planet. Space Sci.* **2006**, *54*, 411–412. [CrossRef]
11. Sauvaud, J.-A.; Maggiolo, R.; Jacquey, C.; Parrot, M.; Berthelier, J.-J.; Gamble, R.J.; Rodger, C.J. Radiation belt electron precipitation due to VLF transmitters: Satellite observations. *Geophys. Res. Lett.* **2008**, *35*, 9. [CrossRef]
12. Graf, K.L.; Inan, U.S.; Piddyachiy, D.; Kulkarni, P.; Parrot, M.; Sauvaud, J.A. DEMETER observations of transmitter-induced precipitation of inner radiation belt electrons. *J. Geophys. Res. Space Phys.* **2009**, *114*, A7. [CrossRef]
13. Inan, U.S.; Piddyachiy, D.; Peter, W.B.; Sauvaud, J.A.; Parrot, M. DEMETER satellite observations of lightning-induced electron precipitation. *Geophys. Res. Lett.* **2007**, *34*, 7. [CrossRef]
14. Anagnostopoulos, G.C.; Vassiliadis, E.; Pulinets, S. Characteristics of flux-time profiles, temporal evolution, and spatial distribution of radiation-belt electron precipitation bursts in the upper ionosphere before great and giant earthquakes. *Ann. Geophys.* **2012**, *55*, 21–36.
15. Shen, X.; Zong, Q.-G.; Zhang, X.M. Introduction to special section on the China Seismo-Electromagnetic Satellite and initial results. *Earth Planet. Phys.* **2018**, *2*, 439. [CrossRef]
16. Huang, J.; Lei, J.; Li, S.; Zeren, Z.; Li, C.; Zhu, X.; Yu, W. The Electric Field Detector (EFD) onboard the ZH-1 satellite and first observational results. *Earth Planet. Phys.* **2018**, *2*, 469. [CrossRef]

17. Zong, J.; Tao, D.; Shen, X. Possible ELF/VLF Electric Field Disturbances Detected by Satellite CSES before Major Earthquakes. *Atmosphere* **2022**, *13*, 1394. [CrossRef]
18. Li, X.Q.; Xu, Y.B.; An, Z.H.; Liang, X.H.; Wang, P.; Zhao, X.Y.; Wang, H.Y.; Lu, H.; Ma, Y.Q.; Shen, X.H.; et al. The high-energy particle package onboard CSES. *Radiat. Detect. Technol. Methods* **2019**, *3*, 22. [CrossRef]
19. Green, J. *NOAA NESDIS-NGDC MEPED Telescope Data Processing*; Technical Report; NOAA: Washington, DC, USA, 2013.
20. Yando, K.; Millan, R.M.; Green, J.C.; Evans, D.S. A Monte Carlo simulation of the NOAA POES Medium Energy Proton and Electron Detector instrument. *J. Geophys. Res.* **2011**, *116*, A10231. [CrossRef]
21. Zhang, Z. (Institute of Crustal Dynamics, China Earthquake Administration, Beijing 100085, China). 2022, Private Communication.
22. Thébault, E.; Finlay, C.C.; Beggan, C.; Alken, P.; Aubert, J.; Barrois, O.; Bertrand, F.; Bondar, T.; Boness, A.; Brocco, L.; et al. International Geomagnetic Reference Field: The 12th generation. *Earth Planets Space* **2015**, *67*, 79. [CrossRef]
23. Alken, P.; Thébault, E.; Beggan, C.D.; Amit, H.; Aubert, J.; Baerenzung, J.; Bondar, T.N.; Brown, W.J.; Califf, S.; Chambodut, A.; et al. International Geomagnetic Reference Field: The thirteenth generation. *Earth Planets Space* **2021**, *73*, 1–25. [CrossRef]
24. McIlwain, C.E. Magnetic coordinates. *Space Sci. Rev.* **1966**, *5*, 585–598. [CrossRef]
25. Ester, M.; Kriegel, H.P.; Sander, J.; Xiaowei, X. A density-based algorithm for discovering clusters in large spatial databases with noise. Technical Report CONF-960830- TRN: 96:005928-0038, 2. In Proceedings of the International Conference on Knowledge Discovery and Data Mining, Portland, OR, USA, 2–4 August 1996.
26. Schubert, E.; Sander, J.; Ester, M.; Kriegel, H.P.; Xu, X. DBSCAN Revisited, Revisited: Why and How You Should (Still) Use DBSCAN. *ACM Trans. Database Syst.* **2017**, *42*, 19. [CrossRef]
27. Sklearn. Sklearn Implementation of DBSCAN Algoritm. Available online: https://scikit-learn.org/stable/modules/generated/sklearn.cluster.DBSCAN.html (accessed on 18 November 2021).
28. Wang, X.; Zhang, L.; Zhang, X.; Xie, K. Application of Improved DBSCAN Clustering Algorithm on Industrial Fault Text Data. In Proceedings of the 2020 IEEE 18th International Conference on Industrial Informatics (INDIN), Warwick, UK, 20–23 July 2020; Volume 1, pp. 461–468. [CrossRef]
29. Zhang, M. Use Density-Based Spatial Clustering of Applications with Noise (DBSCAN) Algorithm to Identify Galaxy Cluster Members. *IOP Conf. Ser. Earth Environ. Sci.* **2019**, *252*, 042033. [CrossRef]
30. Nakamura, R.; Kamei, K.; Kamide, Y.; Baker, D.N.; Blake, J.B.; Looper, M. SAMPEX observations of storm-associated electron flux variations in the outer radiation belt. *J. Geophys. Res. Space Phys.* **1998**, *103*, 26261–26269. [CrossRef]
31. Matzka, J.; Stolle, C.; Yamazaki, Y.; Bronkalla, O.; Morschhauser, A. The Geomagnetic Kp Index and Derived Indices of Geomagnetic Activity. *Space Weather* **2021**, *19*, e2020SW002641. [CrossRef]
32. Despirak, I.V.; Lyubchich, A.A.; Kleimenova, N.G.; Gromova, L.I.; Gromov, S.V.; Malysheva, L.M. Geomagnetic Effects of the Supersubstorms during the Magnetic Storm of March 9, 2012. *Bull. Russ. Acad. Sci. Phys.* **2021**, *85*, 246–251. [CrossRef]
33. Newell, P.T.; Gjerloev, J.W. Evaluation of SuperMAG auroral electrojet indices as indicators of substorms and auroral power. *J. Geophys. Res. Space Phys.* **2011**, *116*, A12211. [CrossRef]
34. Love, J. Magnetic monitoring of earth and space. *Phys. Today* **2008**, *61*, 31. [CrossRef]